

## **Geostatistical characterisation of internal structure of mass-transport deposits from seismic reflection images and borehole logs**

This manuscript is a pre-print submitted to EarthArXiv. The manuscript has been formally accepted for publication in Geophysical Journal International.

---

Please feel free to contact any of the authors, we welcome feedback:

Jonathan Ford ([jford@inogs.it](mailto:jford@inogs.it))

Angelo Camerlenghi ([acamerlenghi@inogs.it](mailto:acamerlenghi@inogs.it))

Istituto Nazionale di Oceanografia e di Geofisica Sperimentale (OGS), Trieste, Italy

# Geostatistical characterisation of internal structure of mass-transport deposits from seismic reflection images and borehole logs

Jonathan Ford\*, Angelo Camerlenghi

*Istituto Nazionale di Oceanografia e di Geofisica Sperimentale (OGS), Trieste, Italy*

December 2019

## SUMMARY

Seismic reflection images of mass-transport deposits often show apparently chaotic, disordered or low-reflectivity internal seismic facies. The lack of laterally coherent reflections can prevent horizon-based interpretation of internal structure. This study instead inverts for geostatistical parameters which characterise the internal heterogeneity of mass-transport deposits from depth-domain seismic reflection images. A Bayesian Markov Chain Monte Carlo inversion is performed to estimate posterior probability distributions for each geostatistical parameter. If the internal heterogeneity approximates an anisotropic von Kármán random medium these parameters can describe the structural fabric of the imaged mass-transport deposit in terms of lateral and vertical dominant scale lengths and the Hurst number (roughness). To improve the discrimination between vertical and lateral dominant scale lengths, an estimate of the vertical dominant scale length from a borehole is used as a prior in the inversion. The method is first demonstrated on a synthetic multi-channel seismic reflection image. The vertical and lateral dominant scale lengths are estimated with lower uncertainty when data from a synthetic borehole data are included. We then apply the method to a real data example from Nankai Trough, offshore Japan, where a large mass-transport deposit is imaged in a seismic profile and penetrated by a borehole. The results of the inversion show a downslope shortening in lateral scale length, consistent with progressive down-slope disaggregation of the mass-flow during trans-

19 port. The dominant scale lengths can be used as a proxy for strain history, which can improve  
20 understanding of post-failure dynamics and emplacement of subaqueous mass-movements,  
21 important for constraining the geohazard potential from future slope failure.

22 **Key words:** submarine landslides – fractals and multifractals – statistical methods

## 23 1 INTRODUCTION

24 Subaqueous mass-movements such as slides, slumps and debris flows are capable of rapidly mo-  
25 bilising and transporting large volumes of sediment in marine and lacustrine slope environments.  
26 They represent a significant geohazard to seafloor infrastructure (Piper et al. 1999; Carter et al.  
27 2014) and to shoreline populations from slide-induced tsunami (Assier-Rzadkiewicz et al. 2000;  
28 Satake 2012). Such events are preserved in the geological record as mass-transport deposits.

29 One focus of geohazard research is to characterise the internal structure of mass-transport de-  
30 posits to better understand the failure dynamics and emplacement of subaqueous mass-movements.  
31 Outcrop studies of exhumed “fossil” mass-transport deposits identify a wide variety of internal  
32 structural fabrics, often showing complex and intense deformation (Pini et al. 2012). Lucente &  
33 Pini (2003) document low-angle thrusting, recumbent folding and progressive down-flow defor-  
34 mation within mass-wasting deposits outcropping in the Marnoso-Arenacea Formation in central  
35 Italy. They also identify kinematic indicators such as asymmetric folding and imbricated duplexes.  
36 Ogata et al. (2014) report soft-sediment deformation structures, slumping and intact blocks of sub-  
37 strate, ripped up and incorporated into the flow during sliding in mass-transport deposits caused  
38 by the collapse of carbonate platforms. These different internal fabrics reflect differing modes of  
39 slope failure, sediment properties and flow dynamics. Internal structure informs strain history and  
40 can thus characterise different flow regimes, enabling division of mass-transport deposits into, for  
41 example, headscarp (extensional), translational and toe (compressive) domains. It can also con-  
42 strain flow kinematics such as run-out distance and flow acceleration, which play a large role in  
43 governing the geohazard potential of an event.

\* jford@inogs.it

44 Acoustic reflection techniques are currently the only geophysical methods able to image sub-  
45 marine mass-transport deposits in-situ. In recent years it has become increasingly common to  
46 study mass-transport deposits using seismic reflection imaging (Martinez et al. 2005; Moscardelli  
47 & Wood 2008; Berndt et al. 2012; Sun et al. 2017). Scientific drilling and coring is also com-  
48 monly performed to estimate geotechnical and petrophysical parameters, such as undrained shear  
49 strength and excess pore pressure (Camerlenghi et al. 2007; Sawyer et al. 2009; Strasser et al.  
50 2011; Dugan 2012). Sediment cores can give a high resolution 3-D reconstruction of strain fabric  
51 within mass-transport deposits (e.g., Strasser et al. 2011), but only for centimeter-scale structure  
52 at single point locations.

53 Bull et al. (2009) catalogue a variety of internal structures seen in mass-transport deposits and  
54 mass-transport complexes from 3-D seismic reflection data. Jackson (2011) documents internally  
55 coherent rafted megablocks emplaced within more chaotic sediments in a mass-transport deposit  
56 from a seismic survey in the Santos Basin, offshore Brazil. Steventon et al. (2019) estimate the  
57 overall strain distribution within a mass-transport complex offshore Uruguay from 3-D seismic  
58 data by identifying individual seismic reflectors and using a backstripping approach.

59 Evidently conventional seismic interpretation techniques (horizon tracking) can be used to in-  
60 terpret internal structure of mass-transport deposits. But this is only possible when i) the deposit  
61 is well-imaged; ii) there is sufficient internal reflectivity to generate seismic reflections and iii) the  
62 scale of internal structure is above the seismic resolution. Very often, however, internal reflectors  
63 can appear chaotic, disordered or low-amplitude (e.g., Diviacco et al. 2006; Moscardelli & Wood  
64 2008; Badhani et al. 2019). In fact, identifying apparently chaotic or transparent seismic facies is a  
65 common way to discriminate failed from unfailed sediments. Many studies use seismic attributes  
66 which are sensitive to discontinuous reflectors, for example the coherence attribute or the chaos at-  
67 tribute (Chopra & Marfurt 2016) to identify mass-transport deposits (Martinez et al. 2005; Gafeira  
68 et al. 2010).

69 This common lack of laterally continuous reflectors within mass-transport deposits makes con-  
70 ventional interpretation of internal structure difficult. Instead, this study aims to characterise in-  
71 ternal structure from seismic reflection data using a geostatistical approach. This avoids the sub-

jectivity inherent to approaches such as horizon tracking and is applicable even when the chaotic nature of a deposit changes laterally, such as a progressive down-slope loss of horizon continuity (e.g., Badhani et al. 2019). The goal is to go beyond using non-dimensional seismic attributes such as the chaos attribute (Chopra & Marfurt 2016) and estimate geostatistical parameters that are quantitative and physically meaningful.

Numerous studies have shown evidence that heterogeneous geology can be described as a band-limited, self-similar medium (sometimes referred to as having fractal characteristics). Examples include i) seafloor bathymetry from multi-beam measurements (Goff & Jordan 1988); ii) exhumed lower continental crust analysed from geological maps (Holliger & Levander 1992); iii) acoustic and elastic numerical modelling of teleseismic waves recorded by earthquake seismology arrays (Frankel & Clayton 1986) and iv) analysis of borehole logs from the upper crust (Holliger 1996; Dolan & Bean 1997; Browaeys & Fomel 2009; Cheraghi et al. 2013). Self-similarity means that the statistical properties of the medium do not change with scale. Specifically, medium properties in power-spectral domain will follow an inverse power-law (Dolan & Bean 1997). In this context, band-limited means that there exists a so-called dominant scale length, the scale above which the medium stops showing self-similar characteristics.

There is also a long history of characterising self-similarity in complex geology using geophysical reflection images. These include i) investigating partial saturation in freshwater aquifers from ground-penetrating radar images (Irving et al. 2009); ii) modelling random media heterogeneities to characterise the seismic response of the crust and mantle at different scales (Carcione et al. 2005) and iii) characterising the geostatistics of complex turbidite systems from 3-D seismic reflection volumes (Caers et al. 2001). Some studies have explored the link between the spatial statistics of the geological medium and the *power spectrum* of the reflected wavefield. Irving & Holliger (2010) present an analytical relationship between band-limited, self-similar random media and a corresponding idealised reflection image. They demonstrate that it is possible to use this relationship to estimate geostatistical parameters characterising the P-wave velocity heterogeneity, such as the aspect ratio of lateral and vertical dominant scale lengths and the Hurst number (a self-similarity coefficient related to the roughness of the medium). This approach relies on the

100 assumption that the reflection image approximates a so-called primary reflectivity section, an ide-  
101 alised seismic image in depth. Irving et al. (2009) demonstrate that this relationship can recover  
102 geostatistical parameters for zero-offset ground-penetrating radar images of shallow, partially sat-  
103 urated aquifers. Scholer et al. (2010) use a similar approach to estimate the correlation structure  
104 of P-wave velocity heterogeneity in the crystalline crust from seismic reflection images, including  
105 a term to compensate for the theoretical lateral resolution limit of migrated reflection images.

106 There is currently little published literature investigating the self-similar characteristics of the  
107 internal structure of mass-transport deposits. Micallef et al. (2008) document scale invariant char-  
108 acteristics of the Storegga Slide, a retrogressive “megaslide” from the mid-Norwegian margin.  
109 They use multi-beam bathymetry data to perform a statistical analysis of sub-bodies within the  
110 slide and infer that the slide exhibits self-organised critical behaviour. They observe an inverse  
111 power-law scaling in their frequency-area distribution and find that headwalls are self-similar from  
112 small to large scales. The authors hypothesise that the fractal statistics of submarine landslides  
113 could be related to the physics of slope failure.

114 This study represents the internal structure of mass-transport deposits as a specific type of  
115 band-limited, self-similar medium, an anisotropic von Kármán random medium (Von Kármán  
116 1948). In two dimensions the random medium can be characterised by three geostatistical pa-  
117 rameters: lateral and vertical dominant scale lengths and the Hurst exponent (roughness). The  
118 dominant scale lengths describe the degree of continuity of the medium in horizontal and vertical  
119 directions respectively. The Hurst number is a dimensionless parameter related to the degree of  
120 self-similarity, which characterises the roughness or texture of the medium (Section 2.1).

121 The aim of this study is to demonstrate a method to constrain the geostatistics of the internal  
122 structure of mass-transport deposits directly from seismic reflection images (after Irving & Hol-  
123 liger 2010). A further goal is to integrate information from a vertical borehole log, where available.  
124 The method is first validated on a synthetic model representing a typical submarine mass-transport  
125 deposit scenario, with a synthetic multi-channel seismic reflection image and a co-located syn-  
126 thetic vertical borehole. Then, the method is applied to a real data case study from the Nankai  
127 Trough, offshore Japan.

## 128 2 METHODOLOGY

129 This method inverts seismic reflection images of mass-transport deposits for geostatistical param-  
 130 eters which can characterise their internal structural fabric. This is achieved by assuming the ve-  
 131 locity heterogeneity within the mass-transport deposit is a random field defined by an anisotropic  
 132 von Kármán random medium. Under this assumption it is straightforward to forward model the  
 133 spatial power spectrum of a corresponding idealised seismic reflection image for a given seismic  
 134 source spectrum. A likelihood function is defined from the residual between the forward modelled  
 135 and observed power spectra. Then, a Bayesian Markov Chain Monte Carlo (MCMC) inversion is  
 136 used to estimate the posterior probability distribution (expected value and uncertainty) for each  
 137 geostatistical parameter. When borehole log information is available, a constraint on the vertical  
 138 dominant scale length and Hurst number can be included in the inversion as a prior.

### 139 2.1 Spatial power spectrum of a random field

140 Here the velocity field,  $v$ , is represented by two components, a smoothly varying background  
 141 component,  $v_0$ , and a zero-mean, small-scale stochastic component,  $v'$ , such that

$$v(x, z) = v_0(x, z) + v'(x, z) \quad (1)$$

142 where  $\frac{v'(x, z)}{v_0(x, z)} \ll 1$  (i.e., the stochastic component is small relative to the background). In gen-  
 143 eral terms, the background velocity is well resolved by geophysical techniques such as travel-time  
 144 tomography. At the bandwidth of conventional marine seismic data (approximately 10-100 Hz),  
 145 however, the small-scale stochastic component generates the vast majority of observed reflec-  
 146 tions in a seismic image. The small-scale stochastic velocity structure is generally poorly resolved  
 147 by seismic reflection experiments except perhaps by full-waveform modelling techniques, which  
 148 can require significant acquisition effort, model conditioning and computational power, with little  
 149 measure of uncertainty in the final result.

150 We make the assumption that the internal heterogeneity (small-scale stochastic structure,  $v'$ )  
 151 of a mass-transport deposit can be approximated as an anisotropic von Kármán random medium.

152 The normalised 2-D spatial power spectrum of an anisotropic von Kármán random medium

153 (Eq. A.1) is

$$P_{v'}(k_x, k_z) = \frac{c}{(k_x^2 a_x^2 + k_z^2 a_z^2 + 1)^{\gamma+1}} \quad (2)$$

154 where  $c$  is a normalising constant,  $k_x$  and  $k_z$  are the horizontal and vertical spatial wavenumbers,  $a_x$   
 155 and  $a_z$  are the dominant lateral and vertical scale lengths and  $\gamma$  is the Hurst number (see Appendix  
 156 A).

## 157 2.2 Forward modelling spatial power spectra

### 158 2.2.1 Migrated seismic image

159 This section follows the methodology presented in Irving & Holliger (2010) which links the ran-  
 160 dom medium parameters to the 2-D power spectrum of a resulting idealised seismic image, some-  
 161 times referred to as a primary reflectivity section (Irving et al. 2009; Scholer et al. 2010). The  
 162 idealised seismic image is a convolutional, zero-offset, normal-incidence, constant density ap-  
 163 proximation. The formulation in depth-domain is:

$$s(x, z) \approx r(x, z) * w(z) * h(x) \quad (3)$$

164 where  $s(x, z)$  is the idealised seismic image in depth,  $r(x, z)$  is the normal-incidence acoustic  
 165 reflectivity,  $w(z)$  is the source wavelet in depth and  $h(x)$  is a horizontal filter to account for the  
 166 lateral resolution of a migrated seismic section (Scholer et al. 2010).

167 The choice of the lateral resolution operator  $h(x)$  is arbitrary but should reflect the lateral  
 168 resolution of the analysed reflection image, which after proper migration is on the order of the  
 169 dominant wavelength of the seismic source (Chen & Schuster 1999). This study follows Scholer  
 170 et al. (2010) in using a Gaussian low-pass filter with width (distance between the two points where  
 171 the filter is 1% of the maximum value) equal to the dominant wavelength:

$$h(x) = \exp\left(\frac{4x^2 \log(0.01)}{\lambda_{\text{dom}}^2}\right). \quad (4)$$

172 Assuming that variation in density is small relative to velocity, the normal-incidence reflectiv-  
 173 ity can be approximated as the derivative of the velocity field:

$$r(x, z) \approx \frac{\partial}{\partial z} v(x, z). \quad (5)$$

174 If reflections from the smooth background velocity,  $v_0$ , are negligible (i.e., the only contribution  
 175 to acoustic reflectivity is the small-scale stochastic component of P-wave velocity) and the source  
 176 wavelet is stationary in depth within the analysis window, the idealised seismic response  $s(x, z)$   
 177 depends only on the stochastic velocity component,  $v'$ :

$$s(x, z) \approx \frac{\partial}{\partial z} v'(x, z) * w(z) * h(x). \quad (6)$$

178 The power spectrum of the seismic image can then be related to the spatial power spectrum of  
 179 the stochastic component by the Fourier transform (Irving & Holliger 2010):

$$P_s(k_x, k_z) = k_z^2 P_{v'}(k_x, k_z) \cdot P_w(k_z) \cdot P_h(k_x) \quad (7)$$

180 where  $P_w$  is the power spectrum of the source wavelet,  $w$ , and  $P_h$  is the power spectrum of the  
 181 lateral resolution filter,  $h$ . It follows that the power spectrum of the seismic image can be directly  
 182 related to the random medium parameters by Eq. 2:

$$P_s(k_x, k_z) = \frac{ck_z^2}{(k_x^2 a_x^2 + k_z^2 a_z^2 + 1)^{\gamma+1}} \cdot P_w(k_z) \cdot P_h(k_x) \quad (8)$$

183 Therefore it is possible to forward model an idealised spatial power spectrum which is compa-  
 184 rable to a window of an observed seismic image under the following assumptions:

185 (i) The analysed window of the observed seismic image approximates a noise-free, zero-offset,  
 186 true-amplitude, convolutional image in depth-domain.

187 (ii) The stochastic component of P-wave velocity heterogeneity,  $v'$ , within the analysed window  
 188 is an anisotropic von Kármán random medium parameterised by  $a_x$ ,  $a_z$  and  $\gamma$ .

189 (iii) The geostatistical parameters and source wavelet are stationary over the analysed window.

190 Only physically realisable models are considered (i.e., dominant scale lengths are non-negative  
 191 and non-zero).

### 192 2.2.2 Borehole log

193 For geohazard studies, for example, borehole logs and cores are often acquired to estimate geotech-  
 194 nical or petrophysical information about the mass-transport deposit (Strasser et al. 2011; Dugan

2012). As these logs have spatial power spectra, we can better constrain geostatistical parameters  
 195 in the direction of the borehole.  
 196

197 Normally, boreholes are approximately vertical, so we can estimate  $a_z$  and  $\gamma$  independently  
 198 from a vertical borehole log alone (Browaeys & Fomel 2009). As borehole logs generally directly  
 199 measure physical parameters we do not need to account for the effect of the seismic source wavelet  
 200 on the geophysical response of the medium. The 1-D form of Eq. 2 is

$$P_b(k_z) = \frac{c}{(k_z^2 a_z^2 + 1)^{\gamma+0.5}} \quad (9)$$

201 where the exponent is modified for a field with Euclidean dimension  $N = 1$  (see Appendix A).

### 202 **2.3 Inversion for geostatistical parameters**

203 This study uses a Bayesian Markov Chain Monte Carlo (MCMC) approach to invert for the geo-  
 204 statistical parameters. The output of the method is a chain of “accepted” models whose joint distri-  
 205 bution is proportional to the posterior probability density of the model. The chain is sampled using  
 206 the Metropolis-Hastings algorithm (detailed in Appendix B). Bayesian approaches have the ad-  
 207 vantage of using prior probability density functions, so prior geological information can be easily  
 208 incorporated if it can be expressed in terms of the model parameters.

209 The likelihood function assumes Laplacian errors (double-exponential distribution) for each  
 210 observation (Mosegaard & Tarantola 1995):

$$L(\mathbf{m}) = \frac{1}{2^N \sigma^N} \exp \left( - \sum_{i=1}^N \frac{|g_i(\mathbf{m}) - \mathbf{d}_{obs,i}|}{\sigma} \right) \quad (10)$$

211 where  $g_i(\mathbf{m})$  represents the forward modelled power spectrum at a given wavenumber,  $\sigma$  is a  
 212 parameter proportional to the magnitude of the combined modelling and observation error,  $N$  is  
 213 the number of observations (total number of points in the observed power spectrum) and  $\mathbf{d}_{obs,i}$  is  
 214 the observed power spectral density for a given wavenumber  $\mathbf{k}_i$ .

215 For this study, the model parameters considered are the geostatistical parameters (lateral and  
 216 vertical dominant scale lengths and the Hurst number) and the error parameter. Multiple paral-  
 217 lel chains are run to measure convergence and ensure that individual chains are well-mixed and  
 218 have truly converged (not simply sampling a low-probability area). For this study, convergence is

219 measured using the Gelman-Rubin statistic (Brooks & Gelman 1998),  $\hat{R}$ , and the weighted mean  
 220 absolute error (WMAE) (Piro et al. 2017). Details of the convergence measures are given in Ap-  
 221 pendix B. Chains are generally assumed to have converged when  $\hat{R} < 1.2$  for all parameters  
 222 (Brooks & Gelman 1998). The weighted mean absolute error should oscillate around 1 when the  
 223 chain is sampling the posterior distribution. To ensure that none of the pre-convergence “burn-in”  
 224 samples are included in the posterior distribution, the first half of each chain is discarded from the  
 225 final posterior distributions.

### 226 2.3.1 *Seismic reflection image*

227 For the chosen window of the 2-D image (the chaotic mass-transport deposit zone), calculate the  
 228 following:

- 229 •  $P_{obs}(k_x, k_z)$ , the 2-D spatial power spectrum of the chaotic window (using a 2-D Fast Fourier  
 230 Transform).
- 231 •  $P_w(k_z)$ , the power spectrum of the seismic source wavelet.
- 232 •  $P_h(k_x)$ , the power spectrum of the lateral resolution filter (Eq. 4).

233 Each iteration of the Metropolis-Hastings algorithm proposes a new candidate model,  $\mathbf{m}' =$   
 234  $[a'_x, a'_z, \gamma', \sigma']$ . For each proposal, forward model the idealised 2-D spatial power spectrum (Eq. 8);  
 235 compute the likelihood of the proposal given  $d_{obs} = P_{obs}(k_x, k_z)$  (Eq. 10) and accept or reject the  
 236 model according to the acceptance criterion (Appendix B).

### 237 2.3.2 *Borehole log*

238 Borehole logs generally attempt to directly measure a physical property of the subsurface. Specifi-  
 239 cally for a sonic log, the measured velocity (or slowness) will include both the background velocity  
 240 trend,  $v_0$ , and the small-scale stochastic component,  $v'$  (Eq. 1). The background trend must be re-  
 241 moved prior to estimation of the dominant scale lengths and Hurst number (Cheraghi et al. 2013).  
 242 The choice of method for de-trending is arbitrary and depends on the complexity of the geology.  
 243 As this study uses relatively small windows of data from borehole logs, we use a simply remove  
 244 the first-order background trend by finding a straight line of best-fit and subtracting it. Borehole

245 logs from different geology may instead require de-trending with a more sophisticated approach  
 246 such as subtracting a low-order best-fit polynomial. The resulting de-trended log should be ap-  
 247 proximately zero-mean and contain only information from the small-scale stochastic component.

248 As for the seismic inversion, the power spectrum of the de-trended borehole log,  $P_b(k_z)$ , should  
 249 be computed using a Fast Fourier Transform.

250 Each iteration of the Metropolis-Hastings algorithm proposes a new candidate model,  $\mathbf{m}' =$   
 251  $[a'_z, \gamma', \sigma']$ . For each proposal, forward model the idealised 1-D spatial power spectrum (Eq. 9);  
 252 compute the likelihood of the proposal given  $d_{obs} = P_b(k_z)$  (Eq. 10) and accept or reject the model  
 253 according to the acceptance criterion (Appendix B).

### 254 2.3.3 Seismic image and borehole log

255 Irving & Holliger (2010) show that under typical experimental conditions, the two dominant scale  
 256 length parameters  $a_x$  and  $a_z$  are strongly dependent on each other, such that it may not be possible  
 257 to resolve each parameter individually from conventional reflection images. However, they show  
 258 analytically that it is possible to reliably estimate the aspect ratio of heterogeneity  $\alpha = \frac{a_x}{a_z}$ . With an  
 259 external estimate of one of the dominant scale lengths, for example  $a_z$  from a vertical borehole  
 260 log, it should be possible to resolve  $a_x$  and  $a_z$  individually.

261 Because the probabilistic inversion approach uses prior probability density functions as an  
 262 input, we can alter these prior probability density functions to reflect our *a priori* knowledge  
 263 of the subsurface. For this inversion, prior probability density functions for the dominant vertical  
 264 scale length,  $a_z$ , and Hurst number,  $\gamma$ , are chosen to be Gaussian, with mean and standard deviation  
 265 calculated from the marginal posterior distributions from the borehole log inversion. The inversion  
 266 proceeds as for the seismic reflection image.

## 267 3 RESULTS

### 268 3.1 Synthetic benchmark – buried submarine mass-transport deposit

269 This synthetic example is designed to benchmark the inversion for a typical marine geohazard  
 270 survey. The data acquisition simulates a multi-channel, marine, towed-streamer acquisition over

271 a chaotic mass-transport deposit body buried under a water layer and heterogeneous sediment  
272 overburden. The aim of this test is to estimate geostatistical parameters from the seismic reflection  
273 image with and without an *a priori* estimate of the vertical dominant scale length from a synthetic  
274 borehole velocity log.

275 The model is divided into two layers, a water layer and a sediment layer, both 350 m thick (see  
276 Fig. 1). Background elastic parameters and geostatistical parameters for the small-scale stochastic  
277 component are given in Table 1. The sediment layer has linearly increasing background P- and  
278 S-wave velocity to approximate the effect of increasing compaction with depth on the seismic  
279 velocities. It includes a zone with significantly shorter lateral dominant scale length and distinct  
280 Hurst number to represent a buried, chaotic mass-transport deposit. Otherwise, the mass-transport  
281 deposit zone has the same background elastic parameters as the host sediment layer. The random  
282 medium zones are realised on a regular (staggered) 2-D mesh (Ikelle et al. 1993).

283 This synthetic benchmark simulates a typical 2-D multi-channel marine acquisition geometry.  
284 The modelled source wavelet is a 40 Hz Ricker. For this synthetic test we use a pseudo-spectral,  
285 isotropic, visco-elastic scheme (Carcione et al. 2005; Carcione 2014) to forward model the seismic  
286 reflection response. Sources and receivers are located in the first row of grid points ( $z = 0$  m). For  
287 this experiment free surface multiples are not modelled; perfectly absorbing boundary conditions  
288 are imposed on all four boundaries of the mesh. P- and S-wave quality factors are set to  $Q_P =$   
289  $Q_S = 10000$  (i.e., negligible attenuation at seismic wavelengths) for all grid points. Full details  
290 of the acquisition and modelling parameters are given in Table 2. In total, 50 shots are modelled  
291 which required 25 hours computation time on a quad-core Intel® Core™ i7-6700 3.40 GHz CPU.

292 As the background velocity model is known and does not vary laterally, the seismic processing  
293 follows a basic marine imaging flow, with a pre-stack true-amplitude Kirchhoff time migration (to  
294  $60^\circ$  maximum angle), outer angle mute (to eliminate refracted arrivals), stack and time-to-depth  
295 conversion using the background P-wave velocity model. The image is cut to the full-fold area,  
296 with maximum depth equal to the maximum depth in the synthetic model (Fig. 2).

### 3.1.1 Borehole log inversion

The synthetic P-wave velocity borehole log is shown in Fig. 2. The window analysed is the mass-transport deposit zone between 500 m and 650 m depth. For the inversion, uniform priors are used:  $0 < a_z \leq 50$  m,  $0 \leq \gamma \leq 1$  and  $0 < \sigma \leq 2$ .

The MCMC is run with 12 parallel chains until  $1 \times 10^4$  samples are accepted to the chain (Table 6). The final Gelman-Rubin statistic  $\hat{R} < 1.02$  for all parameters. The WMAE begins to oscillate around 1 after approximately 200 accepted samples.

Marginal posterior probability distributions for  $a_z$ ,  $\gamma$  and  $\sigma$  are shown in Fig. 3. Summary statistics of the distributions are shown in Table 3. Both geostatistical parameters are centered closed to their true values.

### 3.1.2 Seismic image inversion

Two inversions were run on the seismic reflection image, with and without estimates of the vertical scale length Hurst number from the borehole as priors. The synthetic seismic image is shown in Fig. 2. The window analysed is the mass-transport deposit zone highlighted in Fig. 1.

For the first inversion (seismic image only), uniform priors are used for all parameters.  $0 < a_x \leq 500$  m,  $0 < a_z \leq 50$  m,  $0 \leq \gamma \leq 1$  and  $0 < \sigma \leq 2$ .

The second inversion (seismic image with borehole) is parameterised as the first, but includes a constraint for  $a_z$  and  $\gamma$  from the borehole inversion results. The prior probability density functions for  $a_z$  and  $\gamma$  are Gaussian, with mean and standard deviation from the results of the borehole-only inversion (Table 3). The priors for  $a_x$  and  $\sigma$  are uniform, as above:  $0 < a_x \leq 500$  m,  $0 < \sigma \leq 2$ . The priors for  $a_z$  and  $\gamma$  are truncated Gaussians: for  $a_z$ , mean 15.9 m and standard deviation 3.5 m (truncated at  $0 < a_x \leq 50$  m); for  $\gamma$ , mean 0.37 m and standard deviation 0.09 m (truncated at  $0 \leq \gamma \leq 1$ ).

Both MCMCs are run with 12 parallel chains until  $1 \times 10^4$  samples are accepted to the chain (Table 6). For the first inversion, the final Gelman-Rubin statistic  $\hat{R} < 1.01$  for all parameters. For the second inversion, the final Gelman-Rubin statistic  $\hat{R} < 1.02$  for all parameters. For both inversions the WMAE begins to oscillate around 1 after approximately 100 accepted samples.

324 Marginal posterior probability distributions for  $a_x$ ,  $a_z$ ,  $\gamma$  and  $\sigma$ , alongside a distribution repre-  
325 senting the aspect ratio of heterogeneity,  $\alpha = \frac{a_x}{a_z}$ , are shown in Fig. 3. Summary statistics of the  
326 distributions are shown in Table 3.

327 With respect to the first inversion (seismic image only) the second inversion (seismic image  
328 with constraint from borehole) shows marginal posterior distributions that are closer to the true  
329 values.

### 330 **3.2 Real data case study – Nankai Trough, offshore Japan**

331 The Nankai Trough (offshore southwest Japan) is an oceanic trench formed by the subduction of  
332 the Philippine plate under the Eurasian plate. Associated accretion, seismicity and slope-steeping  
333 have resulted in significant mass-wasting during the last 3 Ma (Strasser et al. 2011; Lackey et al.  
334 2018). A large mass-transport deposit is identified in a 3-D seismic volume (Fig. 4). Here we  
335 consider a 2-D profile extracted from the 3-D volume, chosen to show the maximum extent and  
336 thickness of the mass-transport deposit. The body has a chaotic internal seismic character, with  
337 little visible coherent structure.

338 The survey acquisition parameters are documented in Table 4 (Uraki et al. 2009). The maxi-  
339 mum observed thickness (at the point where the mass-transport deposit intersects the edge of the  
340 seismic volume) is approximately 180 m (Strasser et al. 2011).

341 Also available are logging-while-drilling borehole logs from nearby International Ocean Dis-  
342 covery Programme (IODP) borehole C0018B (Expedition 338, Henry et al. 2012), which pene-  
343 trates the mass-transport deposit (Fig. 4). No sonic log was acquired, so the gamma ray log is used  
344 to estimate the vertical dominant scale length and Hurst number. Whilst the gamma ray log is not a  
345 measure of the P-wave velocity, it is sensitive to changes in lithology (specifically shale fraction),  
346 which should correlate well with the P-wave velocity. It is expected that both gamma ray and sonic  
347 velocity logs should have similar geostatistics within a local interval of a 1-D borehole log.

### 3.2.1 Borehole log inversion

The gamma ray log from IODP borehole C0018B is shown in Fig. 4. The analysis window is the mass-transport deposit zone between 3235 m and 3295 m. For the inversion, uniform priors are used:  $0 < a_z \leq 50$  m,  $0 \leq \gamma \leq 1$  and  $0 < \sigma \leq 2$ .

The MCMC is run with 12 parallel chains until  $5 \times 10^4$  samples are accepted to the chain (Table 6). The final Gelman-Rubin statistic  $\hat{R} < 1.01$  for all parameters. The WMAE begins to oscillate around 1 after approximately 50 accepted samples.

Marginal posterior probability distributions for  $a_z$ ,  $\gamma$  and  $\sigma$  are shown in Fig. 5. Summary statistics of the distributions are shown in Table 5.

### 3.2.2 Seismic image inversion

Two analysis windows are used on the seismic image, in the down-slope and mid-slope parts of the mass-transport deposit (Fig. 4). Both windows have the same dimensions (1000 m by 60 m). The down-slope window is located toward the toe of the mass-transport deposit. The mid-slope window is located relatively further up-slope, in the more proximal part of the mass-transport deposit. Two inversions are run for each window, with and without estimates of the vertical scale length  $a_z$  and Hurst number  $\gamma$  from the borehole log.

For the first inversions (seismic image only), uniform priors are used:  $0 < a_x \leq 500$  m,  $0 < a_z \leq 50$  m,  $0 \leq \gamma \leq 1$  and  $0 < \sigma \leq 2$ .

The second inversions (seismic image with borehole) are parameterised as the first, but include a constraint from the borehole log inversion results (Table 5). The prior for  $a_x$  is uniform, as above:  $0 < a_x \leq 500$  m. The priors for  $a_z$  and  $\gamma$  are Gaussian, fit to the marginal posterior probability distributions from the borehole-only inversion: for  $a_z$ , mean 5.3 m and standard deviation 1.3 m; for  $\gamma$ , mean 0.41 m and standard deviation 0.13 m.

Marginal posterior probability distributions for  $a_x$ ,  $a_z$ ,  $\gamma$  and  $\sigma$ , alongside a distribution representing the aspect ratio of heterogeneity  $\alpha = \frac{a_x}{a_z}$ , are shown in Fig. 6 for both zones. Summary statistics of the distributions are shown in Table 5.

With respect to the first inversion (seismic image only), the second inversion (seismic image

with borehole) shows better-constrained (lower standard deviation) marginal distributions for  $a_x$ ,  $a_z$  and  $\gamma$ . The marginal distributions for the down-slope zone show a notably smaller mean  $a_x$  and  $\alpha$  compared to the mid-slope zone, while maintaining similar distributions for  $a_z$ .

## 4 DISCUSSION

This study applies a geostatistical inversion to characterise the internal structure of mass-transport deposits from seismic reflection images, with and without a constraint from a borehole log. We first demonstrate the method on a synthetic model representing a typical buried submarine mass-transport deposit scenario and then on a real data case study from the Nankai Trough, offshore Japan. The method gives probabilistic estimates of lateral and vertical dominant scale lengths and the Hurst number of the internal heterogeneity. To the authors' knowledge, this is the first time that this technique has been validated with a synthetic test on multi-channel, stacked seismic reflection data. This is also the first published example demonstrating how to condition the inversion using priors derived from a vertical borehole log in order to better constrain the lateral and vertical dominant scale lengths. We suggest that this technique could be a useful tool to better constrain internal structure of mass-transport deposits as it can be applied even to chaotic seismic reflection images of mass-transport deposits, which are common but difficult to interpret using conventional horizon-tracking methods.

### 4.1 Synthetic inversion results

For the inversion performed on the synthetic seismic image with uniform priors, the estimated aspect ratio of heterogeneity,  $\alpha = \frac{a_x}{a_z}$ , is close to the true model value (Fig. 3). This result is expected from previous studies, which suggest that the 2-D power spectrum (equivalently the 2-D autocorrelation function) is strongly sensitive to the aspect ratio of heterogeneity rather than to the individual dominant scale lengths or the Hurst number (Irving et al. 2009; Scholer et al. 2010; Irving & Holliger 2010). This synthetic test, however, shows relatively good resolution of separate lateral and vertical scale lengths from the seismic image alone. The Hurst number is still poorly constrained. Repeating the inversion with priors for vertical scale length and Hurst number esti-

401 mated from a synthetic borehole log improves the result, but only slightly. This is in contrast to  
 402 the conclusions of Irving & Holliger (2010), who predict that the 2-D power spectrum should be  
 403 sensitive only to the aspect ratio of heterogeneity. Our result is likely because the bandwidth of  
 404 the seismic source overlaps both the “white noise” and self-similar parts of the random medium  
 405 in power-spectral domain for this test. Another contributing factor is that this is a synthetic ex-  
 406 periment. Seismic images created from field data contain noise from i) environmental noise ii)  
 407 instrument noise iii) multiple arrivals and iv) processing artefacts. Future studies should investi-  
 408 gate the reliability of this method to discriminate lateral and vertical dominant scale lengths under  
 409 a range of noise conditions and source bandwidths, with respect to the spatial power spectrum of  
 410 the medium.

## 411 4.2 Nankai Trough case study inversion results

412 For the Nankai Trough experiment we consider two identically-sized data windows, a down-slope  
 413 zone and a mid-slope zone (Fig. 4). The down-slope zone is located towards the toe of the mass-  
 414 transport deposit. The mid-slope zone is more proximal, located toward the middle of the deposit.  
 415 The seismic character in both windows is chaotic, lacking laterally coherent seismic reflectors.

416 First, we invert for the geostatistical parameters in both windows with uniform priors (Fig. 6).  
 417 In the down-slope zone, the aspect ratio of heterogeneity,  $\alpha$ , is significantly smaller than in the  
 418 mid-slope zone. Including priors for  $a_z$  and  $\gamma$  based on the nearby IODP borehole C0018B (Fig.  
 419 4), we still see a reduction in  $\alpha$  from mid-slope to down-slope, but we see the distributions for  
 420 lateral and vertical dominant scale lengths,  $a_x$  and  $a_z$ , are much better constrained.

421 Mass-transport deposits often show extensional structures near the headwall, little deformation  
 422 in the central translational zone and compressional structures in the toe region, where the flow may  
 423 be confined (Fig. 7). The observed reduction in lateral dominant scale length from mid-slope to  
 424 down-slope is consistent with this interpretation of the mass-transport deposit. More compression  
 425 will result in increased stratal disruption, giving a shorter lateral dominant scale length compared  
 426 to relatively undeformed sediments. Alternatively, the reduction in lateral dominant scale length  
 427 could be due to progressive down-slope deformation of the mass-flow (Lucente & Pini 2003). Both

428 models could explain the reduction in lateral dominant scale length and aspect ratio of heterogene-  
429 ity.

430 The velocity heterogeneity within the mass-transport deposit should be closely related to litho-  
431 logical heterogeneity. For mass-transport scenarios, this heterogeneity could be predominantly due  
432 to included megaclasts, intact blocks or intense folding from stratal disruption. The observed re-  
433 duction in lateral scale length is consistent with most conceptual models of the variation in internal  
434 structure from proximal to distal within the depositional part of mass-transport deposits (e.g., Bull  
435 et al. 2009, see Fig. 7).

### 436 **4.3 Internal structure from geostatistical parameters**

437 How should these geostatistical parameters be interpreted in the context of mass-transport de-  
438 posits? These parameters are abstract and set in terms of a statistical model, not in terms of  
439 geological structure. We suggest that the dominant scale lengths can be proxies for relative de-  
440 formation from both mass-transport processes and tectonic stresses. Increasing deformation (e.g.,  
441 folding from compression, reduction in size of intact blocks due to progressive disaggregation)  
442 should reduce the lateral dominant scale length and also the aspect ratio of heterogeneity.

443 Here we only consider heterogeneity of the P-wave velocity field, as we believe this should cap-  
444 ture much of the geological heterogeneity that controls the seismic response. In fact, this method  
445 could be used to constrain any kind of geological heterogeneity, so long as it can be related to the  
446 acoustic impedance (the idealised seismic image approximation only models normal-incidence  
447 reflections). For the mass-transport deposit case, for example, one could consider the geological  
448 medium as a mixture of two component lithologies with distinct acoustic impedances (e.g., ma-  
449 trix and clasts). Thus estimating the geostatistical parameters can inform the geostatistics of the  
450 geology directly.

451 For unfailed sediments, one would expect very long lateral dominant scale lengths due to the  
452 presence of laterally continuous beds. After failure, sediments may become deformed due to shear-  
453 ing and disaggregation, reducing the lateral dominant scale length. Therefore the lateral dominant  
454 scale length is a useful structural parameter that can be a proxy for lateral shortening from de-

455 formation. The vertical dominant scale length is more closely related to the average thickness of  
456 beds, and therefore may be less affected by mass-transport.

#### 457 **4.4 Limits in generalisation**

458 Using a synthetic example we show that an idealised seismic image approximation (Section 2.2.1)  
459 is valid for one multi-channel marine seismic experiment, with a specific overburden and seismic  
460 character. This allows a computationally inexpensive inversion method (Table 6) to estimate ran-  
461 dom medium parameters from a window of a reflection image. The validity of the approximation  
462 will depend on the local geology and on the seismic imaging performed. Multiple scattering, atten-  
463 uation and seismic noise will all reduce the validity of the idealised seismic image approximation.

464 The method presented in this study uses the spatial power spectrum to evaluate random me-  
465 dia models and to estimate the misfit between a corresponding theoretical and observed seismic  
466 reflection image. For a given spatial power spectrum there exist infinite physical realisations of  
467 the corresponding random medium. It is important to note that this method only constrains the  
468 statistics of the heterogeneity, not the medium properties directly. It is possible that there are better  
469 statistical representations, especially for small window sizes which may suffer from edge-effects  
470 from the Fast Fourier Transform when calculating the power spectrum. Some previous studies  
471 have used the autocorrelation function instead (e.g., Irving et al. 2009; Scholer et al. 2010).

472 This study only considers 2-D seismic profiles. Mass-transport is an inherently 3-D geological  
473 process, so strong lateral heterogeneity observed in the plane of the profile implies that strong  
474 heterogeneity perpendicular to the profile is also likely. This 3-D heterogeneity could generate  
475 strong out-of-plane reflections. For a chaotic seismic reflection image, it may be impossible to  
476 identify or remove these out-of-plane reflections during imaging or interpretation. It is presently  
477 unclear how the results of the inversion may be affected if these spurious reflections contaminate  
478 the analysis window. This topic could be addressed in a future 3-D numerical modelling study by  
479 performing geostatistical inversion on 2-D profiles which include out-of-plane reflections.

480 Is the anisotropic von Kármán random medium a suitable statistical representation of the in-  
481 ternal structure of mass-transport deposits? There exist many studies suggesting that geology in

482 general has fractal-like properties (band-limited self-similarity; e.g., Goff & Jordan 1988; Turcotte  
483 1997; Browaeys & Fomel 2009; Nelson et al. 2015). There exist, however, few studies investigating  
484 the fractal properties of internal structure of mass-transport deposits (Micallef et al. 2008). Anal-  
485 ysis of mass-transport deposits in outcrop is necessary to determine an anisotropic von Kármán  
486 random medium could be a broadly applicable geostatistical model.

487 The formulation used in this study (Eq. 2) assumes no dominant dip direction. This could be  
488 reasonable for mass-transport deposits deposited in the deep ocean, for example, but not if there  
489 has been post-depositional deformation from tectonics. In future work it should be straightforward  
490 to include dominant dip direction as an extra parameter in the inversion (see Yuan et al. 2014, for  
491 an example).

## 492 **5 CONCLUSIONS**

493 In this study we demonstrate a method to invert for geostatistical parameters (lateral and vertical  
494 dominant scale lengths and Hurst number) which can describe the internal structure of mass-  
495 transport deposits from chaotic multi-channel seismic reflection images and borehole logs. This  
496 approach assumes that the internal structure can be approximated as an anisotropic von Kármán  
497 random medium (Irving & Holliger 2010). The results are probability distributions which provide  
498 the expected value and uncertainty of each geostatistical parameter.

499 The method is first validated on a synthetic scenario containing a buried chaotic body, repre-  
500 senting a submarine mass-transport deposit, imaged with a typical multi-channel marine seismic  
501 acquisition and penetrated by a synthetic borehole. When the seismic image is inverted with a  
502 constraint from the borehole, lateral and vertical dominant scale lengths and Hurst number can be  
503 recovered.

504 The method is then applied to a real data case study from Nankai Trough (offshore Japan).  
505 The data considered are a seismic reflection profile and the gamma ray log from a borehole which  
506 penetrates a thick mass-transport deposit. We see a reduction in lateral dominant scale length from  
507 mid-slope to down-slope part of the mass-transport deposit. This is consistent with progressively  
508 increasing deformation due to disaggregation or compression towards the toe of the slide.

509 Geostatistical inversion is a useful new tool to constrain the internal structure of mass-transport  
510 deposits from seismic reflection data. The geostatistical parameters can be used to validate con-  
511 ceptual models of internal structure and as a proxy for varying strain or degree of deformation in  
512 different domains of the slide, even when the seismic image appears chaotic or reflections lack  
513 the continuity required for horizon-tracking approaches. The lateral dominant scale length in par-  
514 ticular could be a good proxy for strain history, as it is strongly related to the degree of sediment  
515 deformation and stratal disruption.

## 516 **ACKNOWLEDGMENTS**

517 The quality of this manuscript was greatly improved thanks to constructive comments from the  
518 reviewers Guillaume Pirot and Jules Browaeys and the Editor, Frederik Simons. We thank Umberta  
519 Tinavella, José Carcione and Aldo Vesnaver for feedback on an early version of this manuscript.  
520 Thanks to Philippe Cance and Davide Gei for providing the pseudo-spectral numerical modelling  
521 code and for discussion on the topic and to Greg Moore (SOEST) for providing the Kumano 3-  
522 D seismic dataset. Jonathan Ford was supported by a Marie Curie Doctoral Fellowship through  
523 the SLATE Innovative Training Network within the European Union Framework Programme for  
524 Research and Innovation Horizon 2020 under Grant Agreement No. 721403.

## 525 **REFERENCES**

- 526 Assier-Rzadkiewicz, S., Heinrich, P., Sabatier, P. C., Savoye, B., & Bourillet, J. F., 2000. Numerical Mod-  
527 elling of a Landslide-generated Tsunami: The 1979 Nice Event, *pure and applied geophysics*, **157**(10),  
528 1707–1727.
- 529 Badhani, S., Cattaneo, A., Dennielou, B., Leroux, E., Colin, F., Thomas, Y., Jouet, G., Rabineau, M., &  
530 Droz, L., 2019. Morphology of retrogressive failures in the Eastern Rhone Interfluve during the Last  
531 Glacial Maximum (Gulf of Lions, Western Mediterranean), *Geomorphology*, p. 106894.
- 532 Berndt, C., Costa, S., Canals, M., Camerlenghi, A., de Mol, B., & Saunders, M., 2012. Repeated slope fail-  
533 ure linked to fluid migration: The Ana submarine landslide complex, Eivissa Channel, Western Mediter-  
534 ranean Sea, *Earth and Planetary Science Letters*, **319-320**, 65–74.
- 535 Brooks, S. P. & Gelman, A., 1998. General Methods for Monitoring Convergence of Iterative Simulations,  
536 *Journal of Computational and Graphical Statistics*, **7**(4), 434–455.

- 537 Browaeys, T. J. & Fomel, S., 2009. Fractal heterogeneities in sonic logs and low-frequency scattering  
538 attenuation, *Geophysics*, **74**(2), WA77–WA92.
- 539 Bull, S., Cartwright, J., & Huuse, M., 2009. A review of kinematic indicators from mass-transport com-  
540 plexes using 3D seismic data, *Marine and Petroleum Geology*, **26**(7), 1132–1151.
- 541 Caers, J., Avseth, P., & Mukerji, T., 2001. Geostatistical integration of rock physics, seismic amplitudes,  
542 and geologic models in North Sea turbidite systems, *The Leading Edge*, **20**(3), 308–312.
- 543 Camerlenghi, A., Urgeles, R., Ercilla, G., & Brückmann, W., 2007. Scientific ocean drilling behind the  
544 assessment of geo-hazards from submarine slides, *Scientific Drilling*, **4**, 45–47.
- 545 Carcione, J. M., 2014. *Wave Fields in Real Media: Wave Propagation in Anisotropic, Anelastic, Porous*  
546 *and Electromagnetic Media*, vol. 38, Elsevier.
- 547 Carcione, J. M., Finetti, I. R., & Gei, D., 2005. Seismic modelling applied to interpretation of a CROP  
548 crustal section in the Adriatic Sea, in *CROP Project: Deep Seismic Exploration of the Central Mediter-*  
549 *anean and Italy*, vol. 1, p. 794, ed. Finetti, I. R., Elsevier.
- 550 Carter, L., Gavey, R., Talling, P., & Liu, J., 2014. Insights into Submarine Geohazards from Breaks in  
551 Subsea Telecommunication Cables, *Oceanography*, **27**(2), 58–67.
- 552 Chen, J. & Schuster, G. T., 1999. Resolution limits of migrated images, *GEOPHYSICS*, **64**(4), 1046–1053.
- 553 Cheraghi, S., Malehmir, A., Bellefleur, G., Bongajum, E., & Bastani, M., 2013. Scaling behavior and the  
554 effects of heterogeneity on shallow seismic imaging of mineral deposits: A case study from Brunswick  
555 No. 6 mining area, Canada, *Journal of Applied Geophysics*, **90**, 1–18.
- 556 Chopra, S. & Marfurt, K., 2016. Understanding the seismic disorder attribute and its applications, *The*  
557 *Leading Edge*, **35**(8), 695–702.
- 558 Diviacco, P., Rebesco, M., & Camerlenghi, A., 2006. Late Pliocene Mega Debris Flow Deposit and  
559 Related Fluid Escapes Identified on the Antarctic Peninsula Continental Margin by Seismic Reflection  
560 Data Analysis, *Marine Geophysical Researches*, **27**(2), 109–128.
- 561 Dolan, S. S. & Bean, C. J., 1997. Some remarks on the estimation of fractal scaling parameters from  
562 borehole wire-line logs, *Geophysical Research Letters*, **24**(10), 1271–1274.
- 563 Dugan, B., 2012. Petrophysical and consolidation behavior of mass transport deposits from the northern  
564 Gulf of Mexico, IODP Expedition 308, *Marine Geology*, **315-318**, 98–107.
- 565 Frankel, A. & Clayton, R. W., 1986. Finite difference simulations of seismic scattering: Implications for  
566 the propagation of short-period seismic waves in the crust and models of crustal heterogeneity, *Journal*  
567 *of Geophysical Research: Solid Earth*, **91**(B6), 6465–6489.
- 568 Gafeira, J., Long, D., Scrutton, R., & Evans, D., 2010. 3D seismic evidence of internal structure within  
569 Tampen Slide deposits on the North Sea Fan: are chaotic deposits that chaotic?, *Journal of the Geological*  
570 *Society*, **167**(3), 605–616.
- 571 Goff, J. A. & Jordan, T. H., 1988. Stochastic Modeling of Seafloor Morphology: Inversion of Sea Beam

- 572 Data for Second-Order Statistics, *Journal of Geophysical Research: Solid Earth*, **93**(B11), 13589–13608.
- 573 Hastings, W. K., 1970. Monte Carlo sampling methods using Markov chains and their applications,  
574 *Biometrika*, **57**(1), 97–109.
- 575 Henry, P., Kanamatsu, T., Moe, K., & the Expedition 333 Scientists, 2012. Proceedings of the Integrated  
576 Ocean Drilling Program Volume 333 Expedition Reports - NanTroSEIZE Stage 2: Subduction Inputs 2  
577 and Heat Flow, **333**, 16.
- 578 Holliger, K., 1996. Upper-crustal seismic velocity heterogeneity as derived from a variety of *P*-wave  
579 sonic logs, *Geophysical Journal International*, **125**(3), 813–829.
- 580 Holliger, K. & Levander, A. R., 1992. A stochastic view of lower crustal fabric based on evidence from  
581 the Ivrea Zone, *Geophysical Research Letters*, **19**(11), 1153–1156.
- 582 Ikelle, L. T., Yung, S. K., & Daube, F., 1993. 2-D random media with ellipsoidal autocorrelation functions,  
583 *Geophysics*, **58**(9), 1359–1372.
- 584 Irving, J. & Holliger, K., 2010. Geostatistical inversion of seismic and ground-penetrating radar reflection  
585 images: What can we actually resolve?, *Geophysical Research Letters*, **37**(21).
- 586 Irving, J., Knight, R., & Holliger, K., 2009. Estimation of the lateral correlation structure of subsurface  
587 water content from surface-based ground-penetrating radar reflection images, *Water Resources Research*,  
588 **45**(12).
- 589 Jackson, C., 2011. Three-dimensional seismic analysis of megaclast deformation within a mass transport  
590 deposit; Implications for debris flow kinematics, *Geology*, **39**, 203–206.
- 591 Lackey, J., Moore, G., & Strasser, M., 2018. Three-dimensional mapping and kinematic characterization  
592 of mass transport deposits along the outer Kumano Basin and Nankai accretionary wedge, southwest  
593 Japan, *Progress in Earth and Planetary Science*, **5**(1), 65.
- 594 Lucente, C. C. & Pini, G. A., 2003. Anatomy and emplacement mechanism of a large submarine slide  
595 within a Miocene foredeep in the northern Apennines, Italy: A field perspective, *American Journal of  
596 Science*, **303**(7), 565–602.
- 597 Mandelbrot, B. B., 1983. *The fractal geometry of nature*, vol. 173, WH freeman New York.
- 598 Martinez, J. F., Cartwright, J., & Hall, B., 2005. 3d seismic interpretation of slump complexes: examples  
599 from the continental margin of Israel, *Basin Research*, **17**(1), 83–108.
- 600 Micallef, A., Berndt, C., Masson, D. G., & Stow, D. A. V., 2008. Scale invariant characteristics of the  
601 Storegga Slide and implications for large-scale submarine mass movements, *Marine Geology*, **247**(1),  
602 46–60.
- 603 Moscardelli, L. & Wood, L., 2008. New classification system for mass transport complexes in offshore  
604 Trinidad, *Basin Research*, **20**(1), 73–98.
- 605 Mosegaard, K. & Tarantola, A., 1995. Monte Carlo sampling of solutions to inverse problems, *Journal of  
606 Geophysical Research: Solid Earth*, **100**(B7), 12431–12447.

- 607 Nelson, C. E., Hobbs, R. W., & Rusch, R., 2015. On the Use of Fractal Surfaces to Understand Seismic  
608 Wave Propagation in Layered Basalt Sequences, *Pure and Applied Geophysics*, **172**(7), 1879–1892.
- 609 Ogata, K., Pogačnik, Z., Pini, G. A., Tunis, G., Festa, A., Camerlenghi, A., & Rebesco, M., 2014. The  
610 carbonate mass transport deposits of the Paleogene Friuli Basin (Italy/Slovenia): Internal anatomy and  
611 inferred genetic processes, *Marine Geology*, **356**, 88–110.
- 612 Pini, G. A., Ogata, K., Camerlenghi, A., Festa, A., Lucente, C. C., & Codegone, G., 2012. Sedimen-  
613 tary Mélanges and Fossil Mass-Transport Complexes: A Key for Better Understanding Submarine Mass  
614 Movements?, in *Submarine Mass Movements and Their Consequences*, pp. 585–594, eds Yamada, Y.,  
615 Kawamura, K., Ikehara, K., Ogawa, Y., Urgeles, R., Mosher, D., Chaytor, J., & Strasser, M., Springer  
616 Netherlands, Dordrecht.
- 617 Piper, D. J. W., Cochonat, P., & Morrison, M. L., 1999. The sequence of events around the epicentre of  
618 the 1929 Grand Banks earthquake: initiation of debris flows and turbidity current inferred from sidescan  
619 sonar, *Sedimentology*, **46**(1), 79–97.
- 620 Pirot, G., Linde, N., Mariethoz, G., & Bradford, J. H., 2017. Probabilistic inversion with graph cuts:  
621 Application to the Boise Hydrogeophysical Research Site, *Water Resources Research*, **53**(2), 1231–1250.
- 622 Satake, K., 2012. Tsunamis Generated by Submarine Landslides, in *Submarine Mass Movements and*  
623 *Their Consequences*, pp. 475–484, eds Yamada, Y., Kawamura, K., Ikehara, K., Ogawa, Y., Urgeles, R.,  
624 Mosher, D., Chaytor, J., & Strasser, M., Springer Netherlands, Dordrecht.
- 625 Sawyer, D. E., Flemings, P. B., Dugan, B., & Germaine, J. T., 2009. Retrogressive failures recorded in  
626 mass transport deposits in the Ursa Basin, Northern Gulf of Mexico, *Journal of Geophysical Research:*  
627 *Solid Earth*, **114**(B10).
- 628 Scholer, M., Irving, J., & Holliger, K., 2010. Estimation of the correlation structure of crustal velocity  
629 heterogeneity from seismic reflection data, *Geophysical Journal International*, **183**(3), 1408–1428.
- 630 Steventon, M. J., Jackson, C. A.-L., Hodgson, D. M., & Johnson, H. D., 2019. Strain analysis of a seismi-  
631 cally imaged mass-transport complex, offshore Uruguay, *Basin Research*, **31**(3), 600–620.
- 632 Strasser, M., Moore, G. F., Kimura, G., Kopf, A. J., Underwood, M. B., Guo, J., & Sreaton, E. J., 2011.  
633 Slumping and mass transport deposition in the Nankai fore arc: Evidence from IODP drilling and 3-D  
634 reflection seismic data, *Geochemistry, Geophysics, Geosystems*, **12**(5), Q0AD13.
- 635 Sun, Q., Alves, T., Xie, X., He, J., Li, W., & Ni, X., 2017. Free gas accumulations in basal shear zones  
636 of mass-transport deposits (Pearl River Mouth Basin, South China Sea): An important geohazard on  
637 continental slope basins, *Marine and Petroleum Geology*, **81**(Supplement C), 17–32.
- 638 Turcotte, D. L., 1997. *Fractals and chaos in geology and geophysics*, Cambridge University Press.
- 639 Uraki, S., Kido, Y., Sanada, Y., Kuramoto, S., Okano, T., Saga, H., Park, J., Moore, G., & Taira, A., 2009.  
640 Kumano-nada 3D seismic data acquisition and processing, *Butsuri Tansa*, **62**, 277–288.
- 641 Von Kármán, T., 1948. Progress in the Statistical Theory of Turbulence, *Proceedings of the National*

<sup>642</sup> *Academy of Sciences of the United States of America*, **34**(11), 530–539.

<sup>643</sup> Yuan, G., Pei-Min, Z. H. U., Hui, L. I., & Xiao-Yong, L. I., 2014. Estimation of 2d Stationary Random

<sup>644</sup> Medium Parameters from Post-Stack Seismic Data, *Chinese Journal of Geophysics*, **57**(4), 450–461.

## APPENDIX A: VON KÁRMÁN RANDOM MEDIA

The power spectrum of a two-dimensional anisotropic von Kármán random medium is given by Goff & Jordan (1988) as

$$P(k_x, k_z) = \frac{4\pi\gamma H^2}{K_\nu(0)} \frac{a_x a_z}{(k_x^2 a_x^2 + k_z^2 a_z^2 + 1)^{\gamma+1}}, \quad (\text{A.1})$$

where  $a_x$  and  $a_z$  are the horizontal and vertical dominant scale lengths,  $\gamma$  is the Hurst number,  $K_\nu$  is the modified Bessel function of the second kind of order  $\nu = \gamma$ ,  $k_x$  and  $k_z$  are the horizontal and vertical wavenumbers and  $H$  is the variance of the random field.

The Hurst number,  $0 \leq \gamma \leq 1$ , describes the roughness of the random field.  $\gamma = 0$  corresponds to a smoothly varying medium.  $\gamma = 1$  corresponds to a rough medium. For  $\gamma = 0.5$  the anisotropic von Kármán random medium becomes equivalent to a random field with exponential autocorrelation (Holliger & Levander 1992). The Hurst number is related to the fractal dimension,  $D$ , by

$$D = N + 1 - \gamma \quad (\text{A.2})$$

where  $N$  is the Euclidean dimension of the medium (Mandelbrot 1983). This is important when comparing e.g., a borehole log (1-D:  $N = 1$ ;  $1 \leq D \leq 2$ ) to a seismic profile (2-D:  $N = 2$ ;  $2 \leq D \leq 3$ ). As such, the power spectrum of a one-dimensional von Kármán random medium becomes

$$P(k_z) = \frac{4\pi\gamma H^2}{K_\nu(0)} \frac{a_z}{(k_z^2 a_z^2 + 1)^{\gamma+0.5}}. \quad (\text{A.3})$$

## APPENDIX B: BAYESIAN MARKOV CHAIN MONTE CARLO INVERSION

The goal of the inversion is to estimate a model  $\mathbf{m} = [a_x, a_z, \gamma, \sigma]$  which describes the geostatistical properties of the medium and the observation and modelling errors. This study uses a Bayesian Markov Chain Monte Carlo (MCMC) approach to obtain probabilistic estimates for each geostatistical parameter. MCMC methods simulate a random walk through the parameter space of the model to sample the joint posterior probability distribution.

Let  $\mathbf{d}_{obs}$  be a vector of observations (for this study the power spectral density at each wavenum-

ber). Bayes' Theorem states

$$p(\mathbf{m}|\mathbf{d}_{obs}) = \frac{p(\mathbf{d}_{obs}|\mathbf{m})p(\mathbf{m})}{p(\mathbf{d}_{obs})} \quad (\text{B.1})$$

where  $p(\mathbf{m}|\mathbf{d}_{obs})$  is the posterior probability density function,  $p(\mathbf{d}_{obs}|\mathbf{m})$  is the likelihood function (the product of the likelihoods of each observation),  $p(\mathbf{m})$  is the prior probability density function for the model parameters and  $p(\mathbf{d}_{obs})$  acts as a normalising constant. Thus

$$p(\mathbf{m}|\mathbf{d}_{obs}) \propto p(\mathbf{d}_{obs}|\mathbf{m})p(\mathbf{m}). \quad (\text{B.2})$$

Therefore the posterior probability density function (left) is proportional to the posterior probability distribution (right).

If the chain has converged (after a so-called "burn-in" period) the distribution of models in the ensemble will be proportional to the joint posterior probability density function. The marginal distributions will be proportional to the marginal posterior probability density functions for each parameter in the model. This allows estimates of most likely values and uncertainties for each parameter from histograms of the accepted models.

For convenience when finding the product of multiple exponential functions, and to avoid numerical underflow when dealing with floating-point numbers close to zero, this study uses the logarithm of the probability. Maximising a log-likelihood is equivalent to maximising the likelihood.

## B1 Metropolis-Hastings algorithm

The Metropolis-Hastings algorithm is a common MCMC method. The method relies on defining a "target" posterior distribution (product of the prior probability density function and the likelihood function, Eq. B.2) and an arbitrary proposal distribution,  $q$ , which is used to propose candidate additions to the chain, conditional on the last accepted sample.

The acceptance ratio is the ratio of the candidate posterior to the previously accepted posterior (Hastings 1970). If acceptance ratio is greater than 1, the candidate is automatically accepted. If not, the candidate is accepted with probability equal to the acceptance ratio.

For this study the proposal distribution,  $q$ , is chosen to be a truncated Gaussian, centered on

691 the  $\mathbf{m}$  and truncated at the minimum and maximum of the uniform distribution for each parameter  
 692 given in Section 2.3. The variance is 1 for the dominant scale length parameters ( $a_x$  and  $a_z$ ), 0.1  
 693 for the Hurst number ( $\gamma$ ) and 0.01 for the error ( $\sigma$ ) parameter.

---

**Algorithm 1** Metropolis-Hastings algorithm for Markov Chain Monte Carlo
 

---

Draw an initial model from the proposal distribution,  $\mathbf{m}_0 \sim q(\mathbf{m})$

Compute the likelihood of the initial model,  $L(\mathbf{m}_0)$

Set  $n = 1$

**while**  $n < n_{\max}$  **do**

    Draw parameters for a new candidate model,  $\mathbf{m}' \sim q(\mathbf{m}_{n-1})$

    Compute the candidate likelihood  $L(\mathbf{m}')$

    Compute the acceptance probability  $\alpha = \min\left(1, \frac{L(\mathbf{m}')p(\mathbf{m}')q(\mathbf{m}_{n-1}|\mathbf{m}')}{L(\mathbf{m}_0)p(\mathbf{m}_{n-1})q(\mathbf{m}'|\mathbf{m}_{n-1})}\right)$

    Draw a random number from uniform distribution  $x \sim U(0, 1)$

**if**  $\alpha \geq x$  **then**

        Accept proposal to chain:  $\mathbf{m}_n = \mathbf{m}'$

$n = n + 1$

**end if**

**end while**

---

## 694 B2 Convergence criteria

695 The Markov Chain is guaranteed to sample the posterior distribution once the chain has converged  
 696 (after the so-called “burn-in” period). One problem with MCMC methods is determining when  
 697 the “burn-in” period has finished, i.e, after which point to start considering samples as part of the  
 698 posterior distribution. Estimating convergence is important as oversampling the chain increases the  
 699 computation time, whilst undersampling the chain may bias the chain towards the starting values  
 700 and not properly sample low probability regions of the posterior.

701 For this study, the Gelman-Rubin statistic (sometimes called the scale-reduction factor),  $\hat{R}$ , is  
 702 calculated (Brooks & Gelman 1998). This involves running several chains in parallel and compar-  
 703 ing the in-chain variance to the between-chain variance for each parameter in the model. For  $m$

704 chains of length  $2n$  accepted samples,  $W$  is the mean variance each chain,  $B$  is the variance of the  
 705 mean of each chain,  $V_h = B + \frac{W(n-1)}{n}$ ,  $\hat{R} = \sqrt{\frac{V_h}{W}}$ .

706 It is commonly considered that chains have converged for a parameter when  $\hat{R} < 1.2$  (Brooks  
 707 & Gelman 1998).

708 The weighted mean absolute error (WMAE) is given as

$$\text{WMAE} = \frac{1}{N} \sum_{i=1}^N \frac{|g_i(\mathbf{m}) - \mathbf{d}_{obs}|}{\sigma} \quad (\text{B.3})$$

709 where  $N$  is the number of observations (number of wavenumber pairs). The WMAE should oscil-  
 710 late around 1 when the chain is properly sampling the posterior distribution (Pirot et al. 2017).

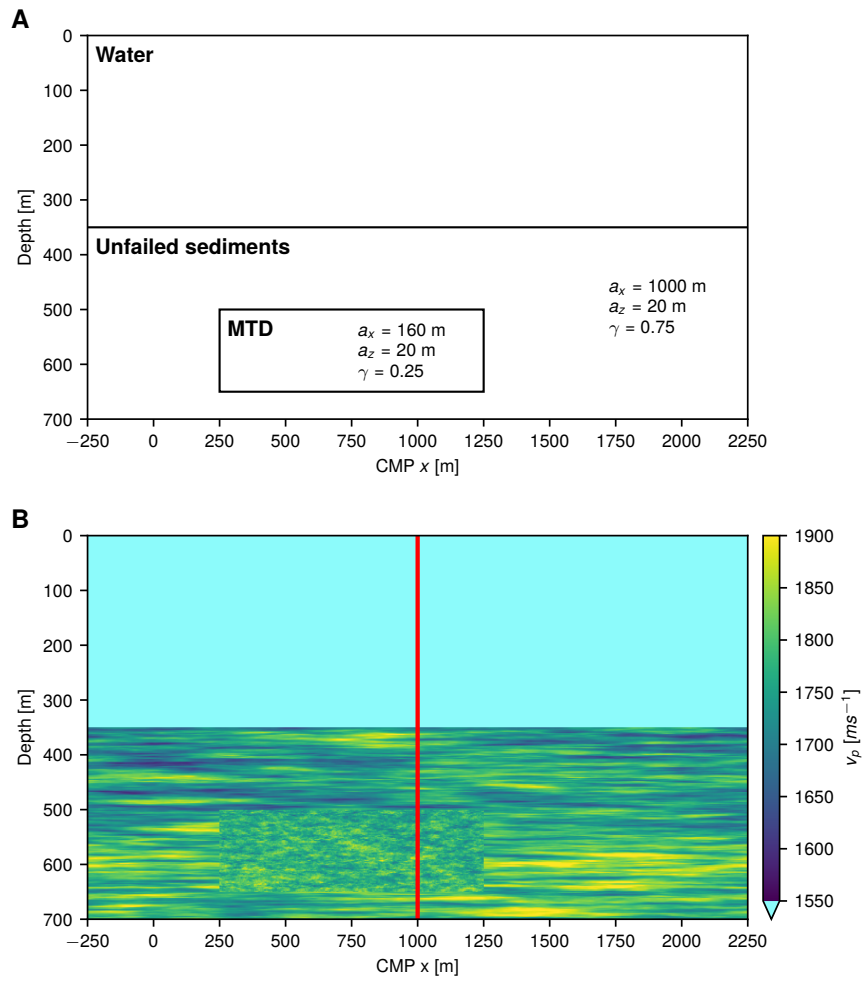


**Figure 1.** Synthetic buried mass-transport deposit (MTD) model. a) Geostatistical parameters: lateral and vertical scale lengths ( $a_x$  and  $a_z$ ) and Hurst number ( $\gamma$ ) for each model zone. The water layer is uniform. Background elastic parameters are given in Table 1. b) P-wave velocity model. The location of the synthetic borehole is shown in red.

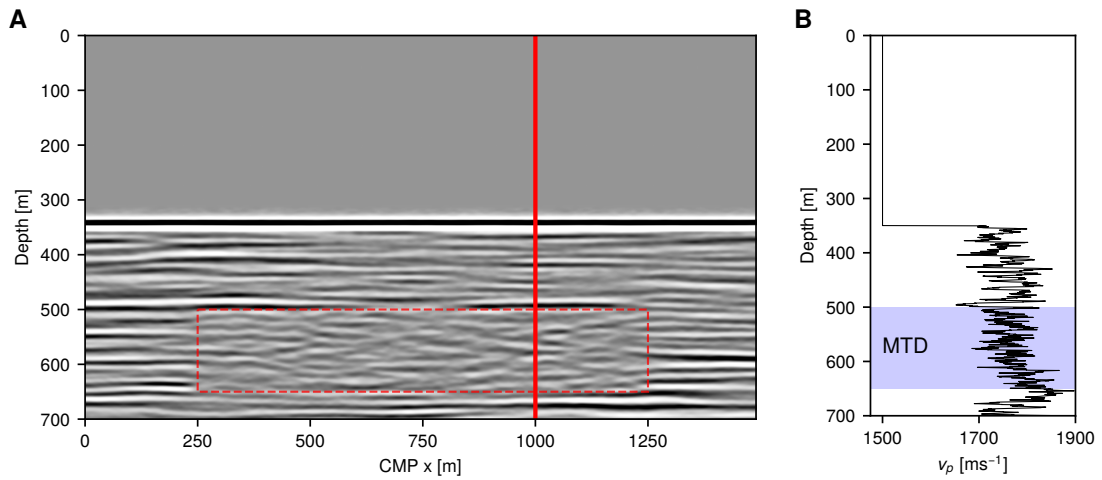


**Figure 2.** Synthetic buried mass-transport deposit modelling results. a) Seismic reflection image in depth-domain (pre-stack time migrated and converted to depth using the smooth background P-wave velocity function in Table 1). Location of the synthetic borehole is shown in solid red. The mass-transport deposit zone (dashed red outline) shows a more disordered, chaotic seismic character compared to the more stratified unfailed sediments. b) P-wave velocity log sampled at 0.25 m.

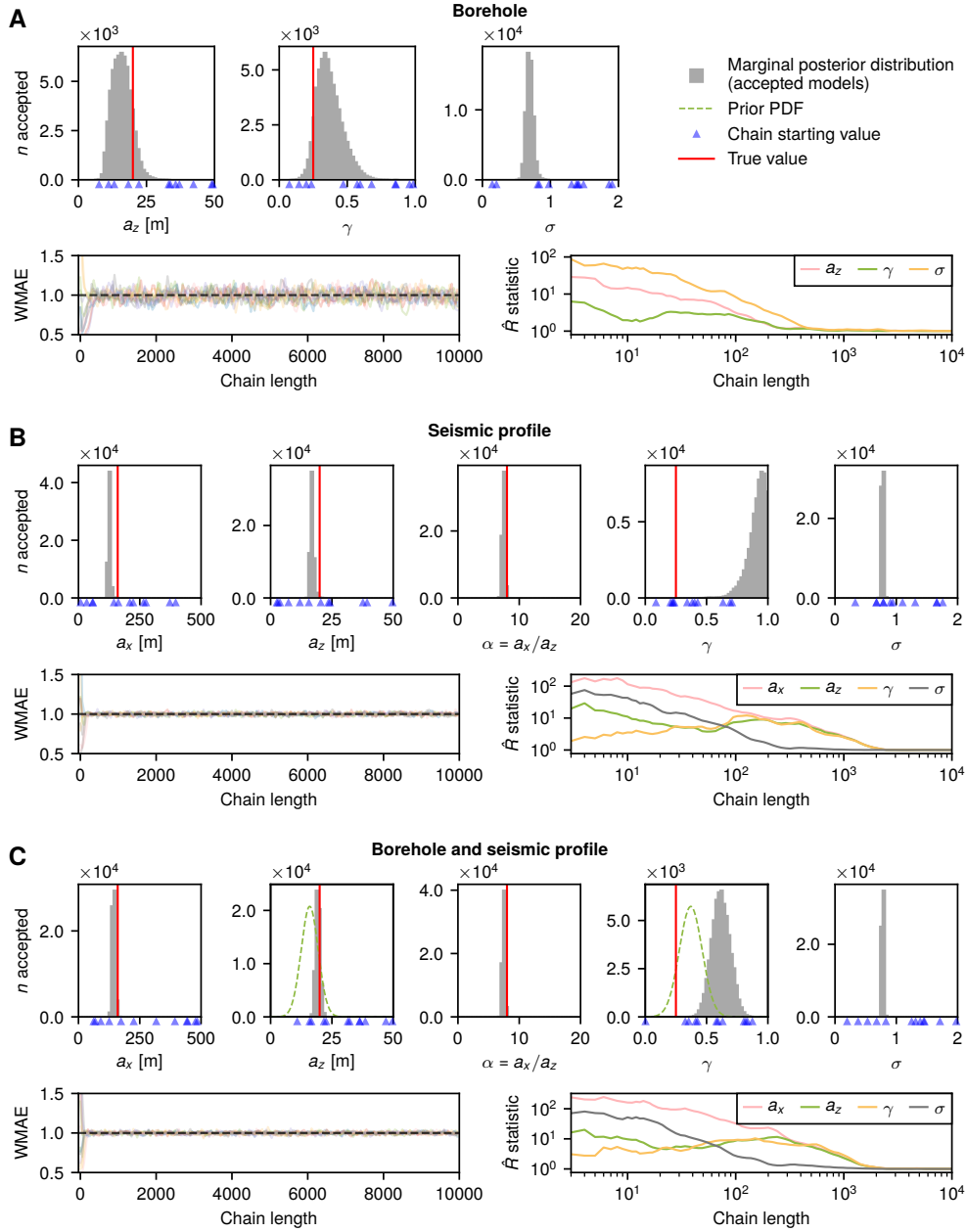


**Figure 3.** Marginal posterior probability distributions for the synthetic buried mass-transport deposit benchmark for dominant lateral and vertical scale lengths,  $a_x$  and  $a_z$ , aspect ratio of heterogeneity,  $\alpha = \frac{a_x}{a_z}$ , Hurst number,  $\gamma$ , and error parameter,  $\sigma$ . True values are shown in red where applicable. Details of priors are given in the text. Convergence measures (WMAE and Gelman-Rubin statistic,  $\hat{R}$ ) are shown for each experiment. a) P-wave velocity log from the synthetic borehole. b) Seismic image. c) Seismic image with constraints on  $a_z$  and  $\gamma$  from the synthetic borehole log.

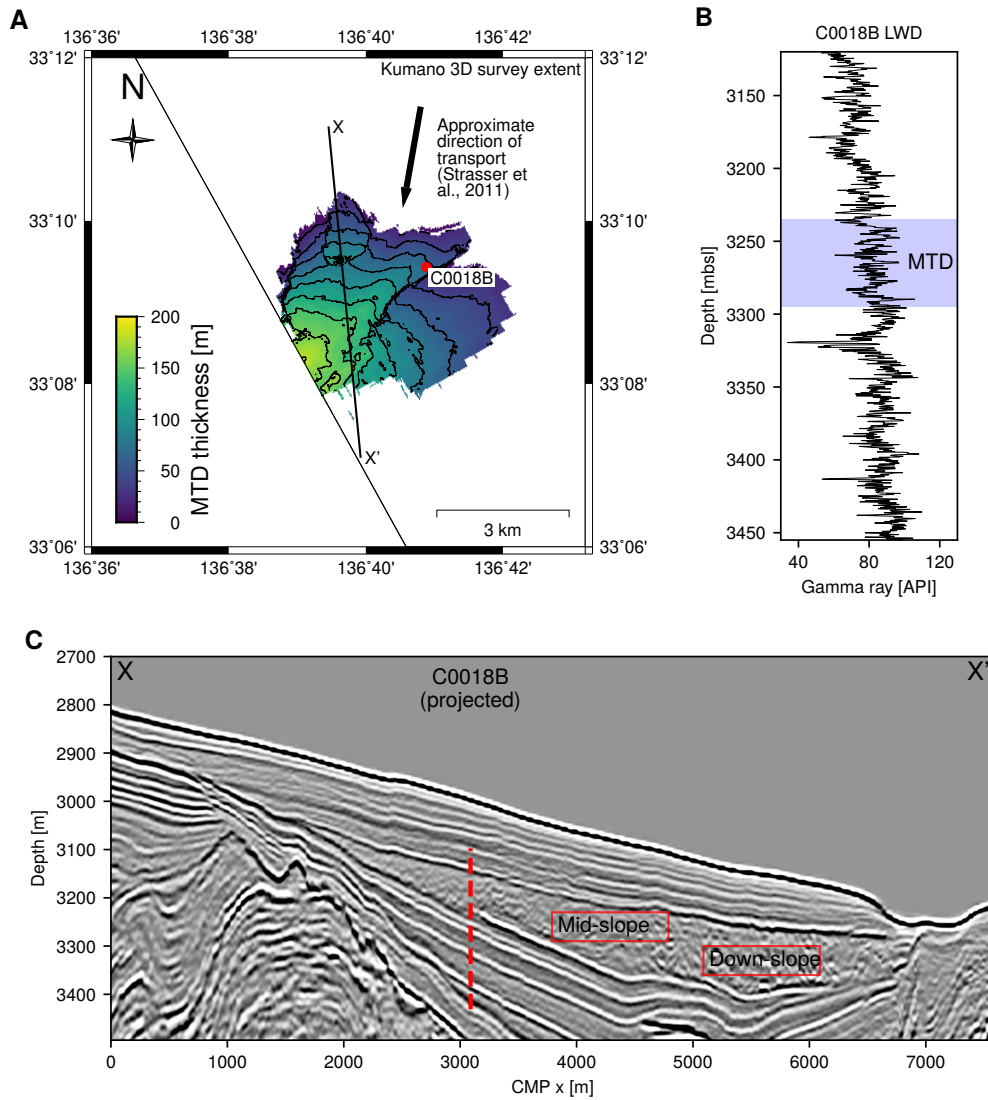


**Figure 4.** Nankai Trough case study data. a) Map showing extent of the Kumano 3-D seismic volume, the thickness of the mass-transport deposit, profile X-X' and IODP borehole C0018B. b) Logging-while-drilling gamma ray log from IODP borehole C0018B, downsampled to 0.25 m, mass-transport deposit (MTD) zone highlighted. c) Seismic reflection profile X-X' (from the 3-D volume) showing a buried mass-transport deposit. The body lacks laterally coherent internal reflections compared to the unfaulted sediments surrounding it. Mid-slope and down-slope zones are indicated alongside the extent of the IODP borehole C0018B (dashed red line) when projected onto the profile.

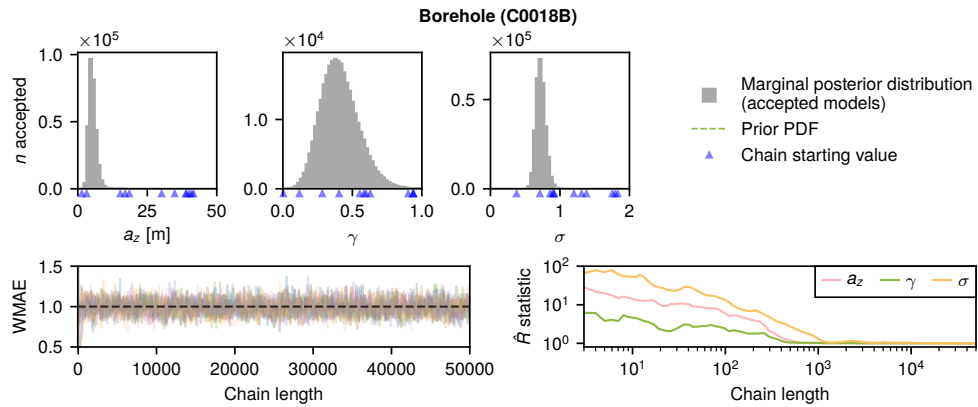


**Figure 5.** Marginal posterior probability distributions for mass-transport deposit (MTD) zone of the gamma ray log from IODP borehole C0018B (Fig. 4) for dominant vertical scale length,  $a_z$ , Hurst number,  $\gamma$ , and error parameter,  $\sigma$ . Details of priors are given in the text. Convergence measures (WMAE and Gelman-Rubin statistic,  $\hat{R}$ ) are shown.

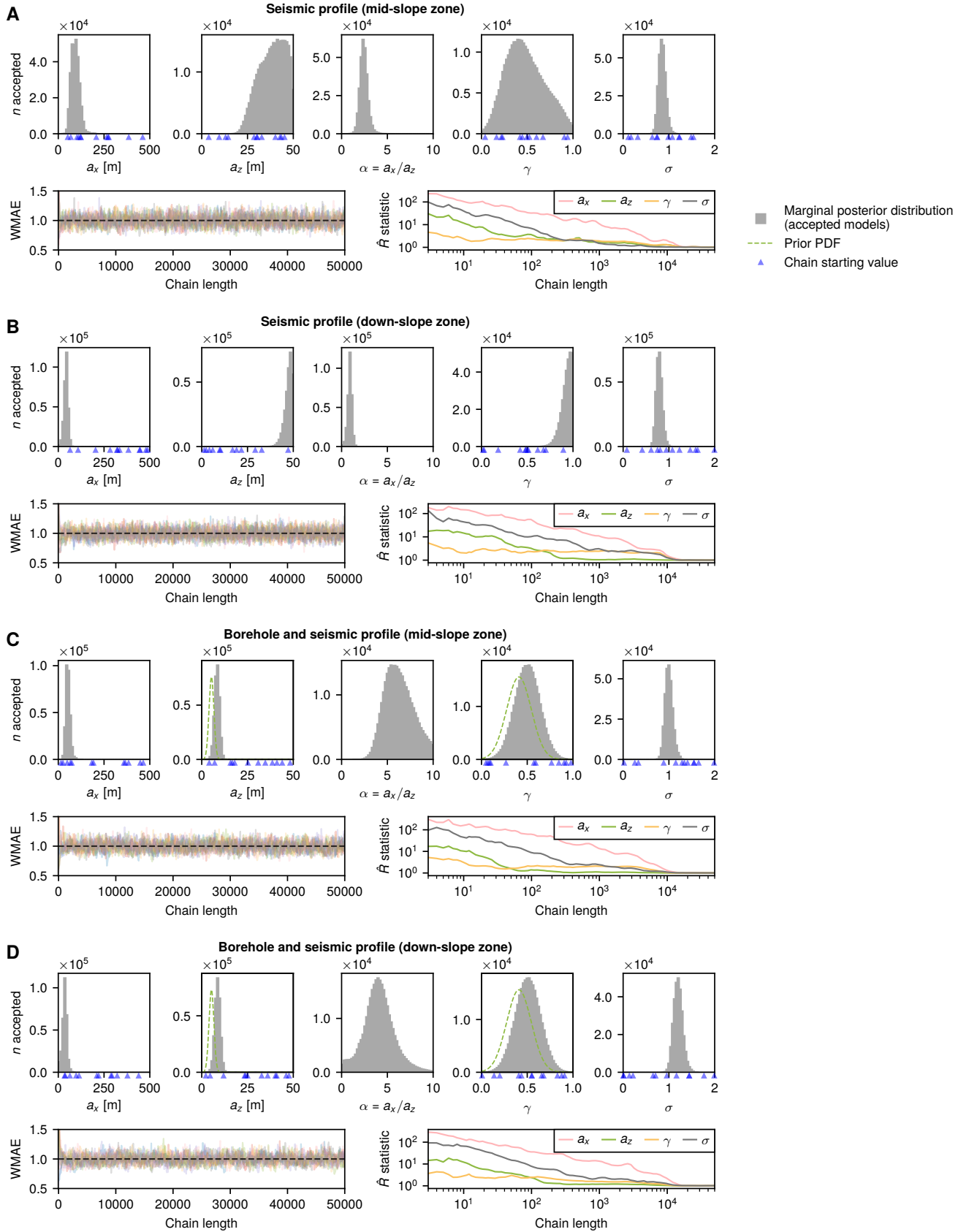


**Figure 6.** Marginal posterior probability distributions for the Nankai Trough case study for dominant lateral and vertical scale lengths,  $a_x$  and  $a_z$ , aspect ratio of heterogeneity,  $\alpha = \frac{a_x}{a_z}$ , Hurst number,  $\gamma$ , and error parameter,  $\sigma$ . Details of priors are given in the text. Convergence measures (WMAE and Gelman-Rubin statistic,  $\hat{R}$ ) are shown for each experiment. a) Mid-slope zone. b) Down-slope zone. c) Mid-slope zone with constraints on  $a_z$  and  $\gamma$  from the borehole log (Fig. 5) d) Down-slope zone with constraints on  $a_z$  and  $\gamma$  from the borehole log (Fig. 5).

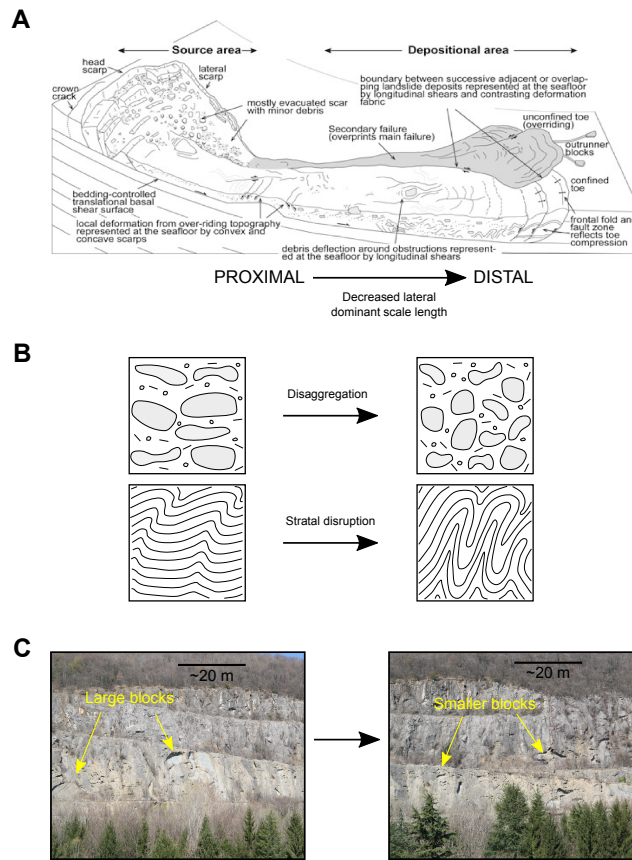


**Figure 7.** a) Schematic diagram showing representative internal structure found within submarine landslides and mass-transport deposits (from Bull et al. 2009). Note increasing deformation due to confinement towards the toe of the slide. b) Illustration of two mechanisms for reducing the lateral dominant scale length by mass-transport – disaggregation of large coherent intact blocks and stratal disruption of soft sediments. In general increased deformation will result in a decrease in lateral dominant scale length (and aspect ratio of heterogeneity). c) Outcrop example of variation in lateral dominant scale length due to a reduction in size of included megaclasts (Vernasso Quarry, NE Italy).

**Table 1.** Background elastic parameters and geostatistical parameters for each unit in the synthetic model (Fig. 1).  $z$  is the depth below the waterbottom,  $v_P$  and  $v_S$  are the P- and S-wave velocities, respectively, and  $\rho$  is the density.

	Background elastic parameters ( $v_0$ )			Geostatistical parameters ( $v'$ )		
	$v_P(z)$ [m s <sup>-1</sup> ]	$v_S(z)$ [m s <sup>-1</sup> ]	$\rho$ [kg m <sup>-3</sup> ]	$a_x$ [m]	$a_z$ [m]	$\gamma$ []
Water	1500	—	1000	—	—	—
Unfailed sediment	$1750 + 0.3z$	$875 + 0.15z$	1600	1200	20	0.75
MTD	$1750 + 0.3z$	$875 + 0.15z$	1600	160	20	0.25

**Table 2.** Synthetic marine multi-channel seismic reflection experiment acquisition and modelling parameters

Synthetic acquisition parameters	
Acquisition geometry	2-D towed streamer
Water depth	350 m
Source wavelet	40 Hz Ricker
Shot interval	40 m
Receiver interval	20 m
Near-offset	25 m
Far-offset	550 m
Nominal midpoint interval	10 m
Fold	
Sampling interval	1 m
Synthetic modelling parameters	
Modelling scheme	Pseudo-spectral (isotropic, visco-elastic)
Boundary conditions	Perfectly absorbing boundaries
Timestep	0.125 ms
Grid spacing	2 m $\times$ 2 m (staggered)

**Table 3.** Summary statistics for the synthetic benchmark marginal posterior probability distributions for dominant lateral and vertical scale lengths,  $a_x$  and  $a_z$ , aspect ratio of heterogeneity  $\alpha = \frac{a_x}{a_z}$ , and Hurst number  $\gamma$ . Mean,  $\mu$ , and standard deviation,  $\sigma$  for each marginal distribution are shown.

Experiment	Mean					Standard deviation				
	$a_x$ [m]	$a_z$ [m]	$\alpha = \frac{a_x}{a_z}$	$\gamma$	$\sigma$	$a_x$ [m]	$a_z$ [m]	$\alpha = \frac{a_x}{a_z}$	$\gamma$	$\sigma$
<b>Synthetic model (true values)</b>	<b>160</b>	<b>20</b>	<b>8</b>	<b>0.25</b>						
Synthetic borehole	—	15.9	—	0.37	0.70	—	3.5	—	0.09	0.05
Seismic image	126	16.9	7.4	0.91	0.78	4	0.7	6.1	0.07	0.01
Seismic image (with synthetic borehole)	144	19.3	7.5	0.62	0.78	6	0.9	6.5	0.07	0.01

**Table 4.** Kumano 3-D marine multi-channel seismic reflection experiment acquisition parameters (Uraki et al. 2009)

---

Kumano 3-D seismic survey acquisition parameters	
Acquisition geometry	3-D towed streamer
Water depth	Approx. 3000 m
Source	Airgun (depth 6 m, dominant frequency 40 Hz)
Shot interval	37.5 m (flip-flop)
Streamers	4 × 4500 m (7 m depth, 150 m separation)
Receiver interval	12.5 m
CMP interval	18.75 m × 12.5 m
Sampling interval	5 m
Nominal fold	30

---

**Table 5.** Summary statistics for the Nankai Trough case study marginal posterior probability distributions for dominant lateral and vertical scale lengths,  $a_x$  and  $a_z$ , aspect ratio of heterogeneity,  $\alpha$ , and Hurst number,  $\gamma$ . Mean,  $\mu$ , and standard deviation,  $\sigma$  for each marginal distribution are shown.

Experiment	Mean					Standard deviation				
	$a_x$ [m]	$a_z$ [m]	$\alpha = \frac{a_x}{a_z}$	$\gamma$	$\sigma$	$a_x$ [m]	$a_z$ [m]	$\alpha = \frac{a_x}{a_z}$	$\gamma$	$\sigma$
Borehole (C0018B)	—	5.3	—	0.41	0.72	—	1.3	—	0.13	0.07
Mid-slope zone	93	38.4	2.4	0.48	0.85	22	6.9	3.2	0.21	0.08
Mid-slope zone (with borehole)	53	8.4	6.4	0.50	1.00	12	1.3	8.6	0.13	0.08
Down-slope zone	42	47.2	0.9	0.93	0.79	11	2.0	5.4	0.06	0.06
Down-slope zone (with borehole)	34	8.6	4.0	0.51	1.20	12	1.4	8.5	0.14	0.10

**Table 6.** Computational cost of each MCMC run. All runs were performed on a quad-core Intel® Core™ i7-6700 3.40 GHz CPU.

Experiment		Parallel chains	Chain length ( $n_{max}$ )	Mean acceptance rate	Execution time
Synthetic	Borehole	12	$1 \times 10^4$	29%	19 mins
	Seismic image	12	$1 \times 10^4$	13%	46 mins
	Seismic image (with borehole)	12	$1 \times 10^4$	10%	60 mins
Nankai Trough case study	Borehole	12	$5 \times 10^4$	48%	23 mins
	Mid-slope zone	12	$5 \times 10^4$	76%	21 mins
	Mid-slope zone (with borehole)	12	$5 \times 10^4$	64%	24 mins
	Down-slope zone	12	$5 \times 10^4$	55%	28 mins
	Down-slope zone (with borehole)	12	$5 \times 10^4$	65%	24 mins